

The Impact of Surface Properties on Downward Surface Shortwave Radiation over the Tibetan Plateau

WANG Leidi^{1,2}, LÜ Daren^{*1}, and HE Qing¹

¹Key Laboratory of Middle Atmosphere and Global Environmental Observation, Institute of Atmospheric Physics, Chinese Academy of Sciences, Beijing 100029

²University of Chinese Academy of Sciences, Beijing 100049

(Received 20 June 2014; revised 11 October 2014; accepted 22 October 2014)

ABSTRACT

The complexity of inhomogeneous surface–atmosphere radiation transfer is one of the foremost problems in the field of atmospheric physics and atmospheric radiation. To date, the influence of surface properties on shortwave radiation has not been well studied. The daily downward surface shortwave radiation of the latest FLASHFlux/CERES (Fast Longwave And Shortwave Fluxes_Time Interpolated and Spatially Averaged/Clouds and the Earth’s Radiant Energy System) satellite data was evaluated against *in situ* data. The comparison indicated that the differences between the two data sets are unstable and large over rugged terrain compared with relatively flat terrain, and the mean absolute error of the satellite products reaches 31.4 W m^{-2} (12.3%) over rugged terrain. Based on the SSF (single satellite footprint)/CERES product, the influence of surface properties on the distribution of downward surface shortwave radiation (DSSR) was analyzed. The influence of surface properties on DSSR over the Tibetan Plateau is about twice as large as that in two other regions located at the same latitude (eastern China–western Pacific and subtropical North Pacific). A simulation was carried out with the help of the I3RC (International Intercomparison of Three-Dimensional Radiation Code) Monte Carlo 3D radiative transfer community model. The results showed that DSSR increases as surface albedo increases. Moreover, the impact of surface albedo on DSSR is larger if the spatial distribution of clouds is more non-uniform. It is hoped that these results will contribute to the development of 3D radiative transfer models and the improvement of satellite inversion algorithms.

Key words: shortwave radiation, surface properties, Tibetan Plateau, satellite remote sensing

Citation: Wang, L. D., D. R. Lü, and Q. He, 2015: The impact of surface properties on downward surface shortwave radiation over the Tibetan Plateau. *Adv. Atmos. Sci.*, **32**(6), 759–771, doi: 10.1007/s00376-014-4131-2.

1. Introduction

Solar radiation is a significant source of heat for the earth–atmosphere system. The heterogeneity of surface solar radiation could affect the radiative energy budget, weather systems and climate change. The solar flux received by the surface involves the attenuation of insolation by scattering and absorption caused by atmospheric gases, aerosols, cloud particles, and surface properties. Among others, surface parameters generally include altitude, gradient, slope direction and surface albedo. Different surface properties result in different dynamic and thermodynamic processes, which influence the exchange of matter and energy between the land surface and the atmosphere. The surface albedo characterizes the surface reflection of solar radiation. It determines energy exchange between the surface and atmosphere, and it is a key factor influencing Earth’s climate system. Even a small change in surface albedo could shift the energy

balance of the earth–atmosphere system, and result in regional and global climate change (Wang et al., 2002; Stroeve et al., 2005). Over the Tibetan Plateau, the mean surface elevation is 4000 m above sea level. Its protruding nature with high elevation and complex surface properties results in equally complex weather and cloud systems over the region. There is a 3D radiative transfer problem in the inhomogeneous surface–atmosphere system. However, most radiative transfer models and satellite inversion algorithms are highly simplified. Compared to atmospheric composition and clouds, the effects of surface properties on downward surface shortwave radiation (DSSR) have not been well studied until now. Thus, it is worth exploring the effects of surface properties on DSSR.

As an important complement to ground observations, satellite remote sensing provides data with preferable continuity and homogeneity in both time and space, and has become an effective way to study surface radiation budgets. However, satellite products may be severely biased due to input data inaccuracy, algorithm errors, and the influence of surface properties and elevation differences (Yang et al.,

* Corresponding author: LÜ Daren
Email: ludr@mail.iap.ac.cn

2006). The complexity of spatial orientation and the optical properties of the surface have so far been investigated in a relatively limited number of radiative transfer schemes (e.g., Dubayah and Rich, 1995; Wang et al., 2005; Liou et al., 2007; Helbig et al., 2009; Lee et al., 2013; Stöckli, 2013). Their effects on the surface solar radiation budget have not been well accounted for in the most widely applied radiative transfer schemes in which the lower boundary is assumed to be unobstructed, horizontal, and homogeneous. Therefore, it is necessary to validate satellite data against in situ observations, because such validations not only guarantee data quality but also provide useful information to improve the retrieval algorithms. Meanwhile, climate simulations require accurate and stable radiation budget data, and the products obtained from space are useful for climate research (Ohring et al., 2005).

The Tibetan Plateau has great impacts on energy and water cycles at both regional and global scales, making it a useful research area for testing the quality of data and the estimation algorithms. Yang et al. (2006, 2008, 2010) assessed the satellite-estimated surface downwelling shortwave irradiance of ISCCP-FD (International Satellite Cloud Climatology Project-Flux Data) and GEWEX-SRB (Global Energy and Water Cycle Experiment-Surface Radiation Budget) by using the in situ data of several surface sites over the Tibetan Plateau. Comparisons indicated that the errors of satellite products are spatially dependent over Tibet, and discrepancies between different products are usually larger in the presence of highly variable terrain. Gui et al. (2009, 2010) compared ISCCP-FD and CERES-FSW (Clouds and the Earth's Radiant Energy System-Monthly Gridded Radiative Fluxes and Clouds) hourly surface solar radiation with ground measurements. The results showed that the accuracy of satellite-estimated data cannot meet the requirements of research communities, and satellite-estimated data over the Tibetan Plateau must be substantially improved, especially for the shortwave components.

Observations show that the downward shortwave radiation over Tibet is much higher than that over sea level along the same latitude (Ma et al., 2005; Wang et al., 2013). In addition to the high elevation, there are several west-east elongated high mountains and many hills leading to the complex terrain. The complex terrain can affect solar radiation in direct (Dubayah and Rich, 1995; Dubayah and Loechel, 1997; Kang et al., 2002; Wang et al., 2005; Ryu et al., 2008; Helbig et al., 2009) and indirect (Kuwahata et al., 2001; Kurosaki and Kimura, 2002) ways. Besides clouds, the leading uncertainties in surface fluxes originate from the surface and near-surface atmospheric properties (Zhang et al., 2006, 2007).

According to the results of a 3D Monte Carlo photon tracing program, the mean surface solar flux over a region with complex topography can deviate from a smooth surface by as much as $10\text{--}50\text{ W m}^{-2}$ for an albedo of 0.2, and the anomalies of solar flux in clear-sky conditions can be as much as 600 W m^{-2} (Liou et al., 2007). Given the altitudinal dependence of DSSR, caution is needed when applying current satellite data to plateau regions. Ground measurements over the Tibetan Plateau can be used as a benchmark for evaluating

satellite algorithms at high elevations (Yang et al., 2006).

Most evaluations of satellite products have been performed in low elevation areas with smooth surfaces, and high accuracy has been shown. As for the quality of satellite products over the Tibetan Plateau, most previous studies have focused solely on relatively short periods of several months, and have not evaluated the latest FLASHFlux (Fast Longwave And Shortwave Fluxes, Time Interpolated and Spatially Averaged)/CERES product. It is unknown to what extent surface properties influence satellite-estimated DSSR. The transfer of shortwave radiation under the co-existence of 3D clouds and complex surface properties still requires exploration.

The remainder of the paper is arranged as follows. Section 2 introduces the datasets and processing used in the study. In section 3, the DSSR from the latest FLASHFlux/CERES data over a whole year is assessed against three ground sites over the Tibetan Plateau, and the impact of surface properties on the satellite-estimated DSSR is analyzed. Then, the shortwave radiation flux transferred through two types of clouds is simulated using a state-of-the-art model. Finally, the overall conclusions of the study and some further discussion are presented in section 4.

2. Materials and methods

2.1. In situ data

In situ observations from three sites are adopted in this study (Fig. 1):

(1) Yangbajain [(30.088°N, 90.540°E); 4350 m]: This site is located on the southern side of Nyainqentanglha Mountain in the center of the Tibetan Plateau. It is annexed to the Institute of High Energy Physics of the Chinese Academy of Sciences.

(2) The Nam Co Monitoring and Research Station for Multisphere Interactions [(30.774°N, 90.988°E); 4730 m]. This site is located on the southeast shore of Nam Co Lake, 220 km away from Lhasa. It was established by the Institute of Tibetan Plateau Research, Chinese Academy of Sciences in 2005.

(3) The Semi-Arid Climate and Environment Observatory of Lanzhou University [known as SACOL; (35.946°N,

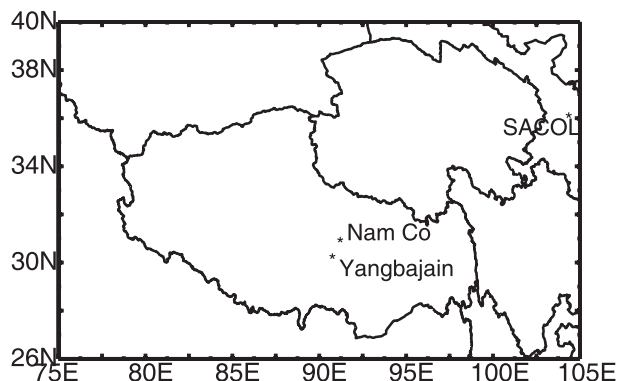


Fig. 1. Locations of the Yangbajain, Nam Co and SACOL sites.

104.137°E); 1965.8 m]. This site is near the city of Lanzhou, on the southern bank of the Yellow River in northwestern China. In particular, this site is very close to the geometric center of China’s mainland.

The values of surface shortwave irradiance were measured by pyranometers at each site [Yangbajain: TBQ-2-B-I, HUATRON, Beijing, China (1-min resolution); Nam Co: Model-CM, Kipp & Zonen, The Netherlands (5-min resolution); SACOL: Model-CM, Kipp & Zonen, The Netherlands (1-min resolution)]. The sensitivity of the TBQ-2-B-I pyranometer is $10.22 \times 10^{-6} \text{ V W}^{-1} \text{ m}^2$. The TBQ-2-B-I pyranometer is comparable to other pyranometers, and is widely used in meteorological stations. All three solar pyranometers were rigorously tested before installation. The time sequence of the *in situ* data is from April 2009 to March 2010 at Yangbajain and Nam Co, and from January 2009 to August 2010 at SACOL. To acquire the best possible data for solar radiation, daily quality assurance checks are essential. The quality control procedures are derived from WMO (World Meteorological Organization) and Geiger et al. (2002) with minor modifications.

2.2. Satellite data

By improving the scene identification and increasing the sensitivity of angular distribution models, CERES improves the TOA flux accuracy for individual cloud types, thereby providing a more reliable dataset for studying radiative processes and radiative forcing by cloud type (Loeb et al., 2003). CERES has four level products. Our work used the SSF (Single Scanner Footprint) product from level 2 and FLASHFlux Version 2G from level 3. The other products after level 2 are based on the level 2 products. The SSF product contains one hour of instantaneous CERES data for a single scanner instrument. The SSF combines instantaneous CERES data with scene information from a higher resolution imager such as VIRS (Visible/Infrared Scanner) on TRMM (Tropical Rainfall Measuring Mission) or MODIS (Moderate-Resolution Imaging Spectroradiometer) on Terra and Aqua. Each SSF granule contains one hour of data, which is approximately two-thirds of an orbit from a single CERES instrument. The width of the SSF swath is limited to the width of the imager swath with which the CERES data were convolved. Each SSF field of view (FOV) represents one scanner measurement. Measurements are taken every 0.01 seconds. According to different algorithms, the SSF can be divided into two products: the “A” model product (Li et al., 1993) and “B” model product (Gupta et al., 2001).

2.3. Methods

The gridded satellite data were bilinearly interpolated onto the locations of the *in situ* data, so the satellite and *in situ* data can be compared. It should be noted that deviation exists in the ground observations themselves, and the validation techniques also produce errors because of the inhomogeneous distribution of meteorological variables. The statistical methods used in this work follow previous studies (Huang, 2004; Houborg et al., 2007; Kim and Liang, 2010; Yang et

al., 2010). The statistics are reported in absolute (W m^{-2}) and relative units (percentage of average measured global irradiance). The statistics in absolute units are given by

$$\text{ME} = \frac{1}{N} \sum_{k=1}^N (e_k - m_k), \tag{1}$$

$$\text{MAE} = \frac{1}{N} \sum_{k=1}^N |e_k - m_k|, \tag{2}$$

and the statistics in relative units are given by

$$\text{ME} = \frac{1}{N} \sum_{k=1}^N \frac{e_k - m_k}{m_k}, \tag{3}$$

$$\text{MAE} = \frac{1}{N} \sum_{k=1}^N \frac{|e_k - m_k|}{m_k}, \tag{4}$$

$$R = \frac{\frac{1}{N} \sum_{k=1}^N (e_k - \bar{e})(m_k - \bar{m})}{\sqrt{\frac{1}{N} \sum_{k=1}^N (e_k - \bar{e})^2} \sqrt{\frac{1}{N} \sum_{k=1}^N (m_k - \bar{m})^2}}, \tag{5}$$

$$\text{RMSD} = \frac{\sqrt{\frac{1}{N} \sum_{k=1}^N (e_k - m_k)^2}}{\frac{1}{N} \sum_{k=1}^N m_k}, \tag{6}$$

where e and m represent satellite predictions and ground measurements, respectively; \bar{e} and \bar{m} are the averages of satellite predictions and ground measurements, respectively; N represents the number of samples; ME represents mean error; MAE represents mean absolute error; R represents the correlation coefficient; and RMSD represents root-mean-square deviation.

In this study we used the I3RC Monte Carlo 3D radiative transfer community model (I3RC-community-monte-carlo). This model has been tested and found to be superior and more efficient in computing the downwelling flux than SHDOM (Spherical Harmonic Discrete Ordinate Method) (Cahalan et al., 2005; Pincus and Evans, 2009). The heart of the model is a monochromatic integrator, and more details can be found in Pincus and Evans (2009). Nevertheless, there are two major limitations of this model: First, the current code cannot solve atmospheric molecular absorption problems. Second, the current code can only deal with Lambertian surfaces. In our study, the simulation used 10^9 photons to guarantee precision, based on the suggestion of Evans and Marshak (2005).

To ensure better accuracy for examining the interplay of the surface, clouds and solar radiation, we performed simulations at a nonabsorbing wavelength of clouds in the visible spectrum ($0.675 \mu\text{m}$) and an absorbing wavelength in the near-infrared spectrum ($2.13 \mu\text{m}$) under different surface albedos without considering the atmosphere. Unfortunately, the topographic effect was not implemented because of the limitation of the current Monte Carlo code. The setting of some basic parameters follows that of Pincus and Evans (2009). For all calculations, the sun azimuth was set to 0° (in this study, 0° means that the sun’s rays are directed from the direction of increasing x), and the sun zenith was set to 30° . In this study, a stratocumulus field (Moeng et al., 1996)

and a cumulus field (Stevens and Lenschow, 2001) are used as the input of the Monte Carlo model. Figure 2 shows the two cloud fields. More information about these two clouds can be found in Wang et al. (2014).

3. Results

3.1. Comparisons of satellite and *in situ* data

First, we plotted the daytime solar radiation against time. Days with a very smooth curve were considered as clear-sky days because clouds lead to clear fluctuation of solar radiation. Figures 3a, c and e show the scatter diagrams for all-sky days and Figs. 3b, d and f for clear-sky days. For all-

sky days, there are large differences between the two products. Among the different sites, the satellite errors are smaller at SACOL, which has a relatively flat surface compared to the other two sites with their rugged terrain. The correlation coefficients between FLASHFlux and the observation are 0.899, 0.884 and 0.966 for Yangbajain, Nam Co and SACOL, respectively. The mean absolute errors of satellite-estimated data are 26.69 W m^{-2} (10.96%), 31.38 W m^{-2} (12.26%) and 18.84 W m^{-2} (15.93%), respectively. The root-mean-square errors for the three sites range from 12.92% to 16.86%.

Under clear-sky conditions (Figs. 3b, d, f), the DSSR results based on the FLASHFlux/CERES products and *in situ* data show a much better relationship than that under all-sky conditions. At Yangbajain and Nam Co, the FLASHFlux

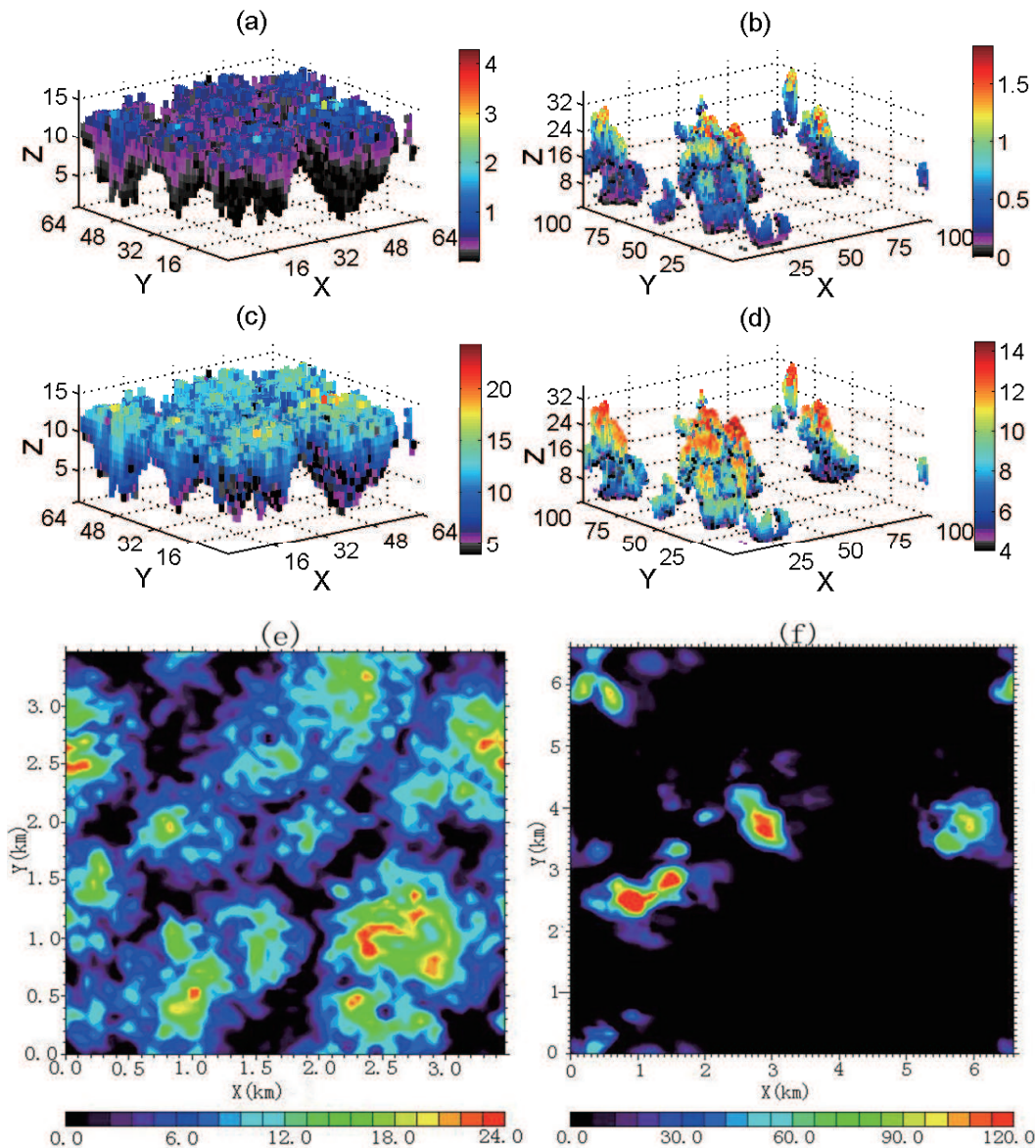


Fig. 2. (a, b) Liquid water content (units: g m^{-3}), (c, d) effective particle radius (units: μm), and (e, f) optical depth (units: 1) at wavelength $0.67 \mu\text{m}$ of (a, c, e) stratocumulus and (b, d, f) cumulus. Note: the photographs corresponding to the cloud optical depth at wavelength $0.67 \mu\text{m}$ were adopted from I3RC: http://i3rc.gsfc.nasa.gov/cases_new.html. [Reprint from Wang et al. (2014)]

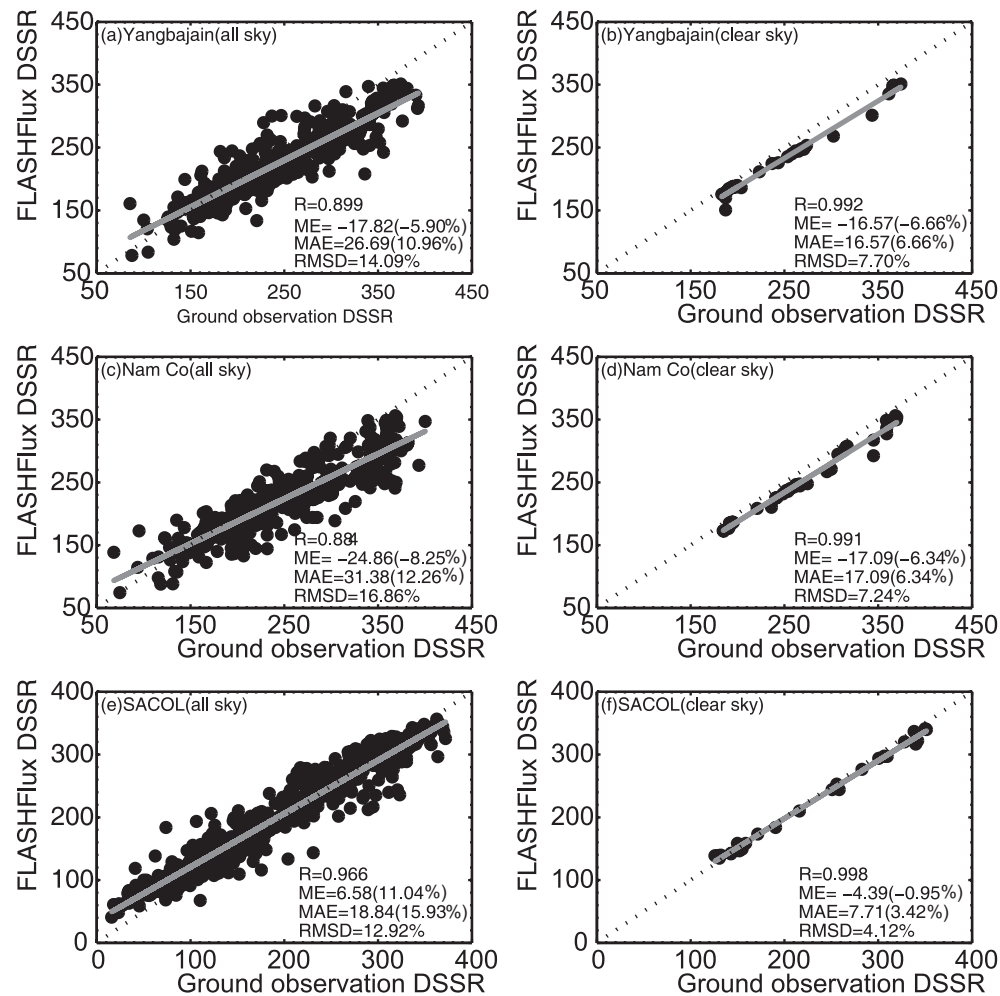


Fig. 3. Scatter diagrams of the DSSR of FLASHFlux/CERES products versus *in situ* observations (units: W m^{-2}): (a, b) Yangbajain; (c, d) Nam Co; (e, f) SACOL. R represents correlation; ME represents mean error; MAE represents mean absolute error; and RMSD represents root-mean-square deviation.

value tends to be lower than ground measurements on every clear-sky day. The mean error is -16.57 W m^{-2} (-6.66%) for Yangbajain, -17.09 W m^{-2} (-6.34%) for Nam Co, and -4.39 W m^{-2} (-0.95%) for SACOL. At the same time, the RMSD is very small, which suggests the difference between the two datasets is very stable. The satellite products are more consistent with surface measurements under cloudless conditions than under all-sky conditions. The differences indicate that the satellite errors partly result from the algorithms, which ignore 3D cloud properties. The quality of the satellite inversion products is spatially dependent, and tends to be better for the area with smooth terrain.

The mean error for all all-sky days is negative at Yangbajain and Nam Co, and positive at SACOL. The positive bias at SACOL site may be mainly attributable to the underestimation of the aerosol amount in the retrieval process, especially for aerosol in the sub-thin-cloud layer (Hayasaka et al., 2006). Very low aerosol optical values have been observed over the Tibetan Plateau because of the sparse population and minimal industrial activity (Cong et al., 2009). Therefore, at

Yangbajain and Nam Co, the DSSR is much less affected by aerosols. The causes of the negative biases at Yangbajain and Nam Co are not immediately obvious. The negative biases may be due to the neglect of 3D radiative effects under the conditions of the heterogeneous clouds and complex surface, satellite overestimation of aerosol optical depth, or other reasons.

But how does the error between satellite and *in situ* measurements differ among the twelve months of the calendar year? Figure 4 shows the MAE and RMSD as a function of the calendar month. The MAE and RMSD vary with month. At Yangbajain, the MAE varies from 7.58% up to 26.56% with the highest value in June, and the RMSD varies from 9.49% up to 18.35% with the highest value in May. At Nam Co, the MAE ranges from 8.69% to 33.82% with the lowest value in January and the highest value in May, and the RMSD ranges from 10.07% to 22.99% with the lowest value in January and the highest value in May. At SACOL, the error changes smoothly throughout the year, except in a few months. There is a

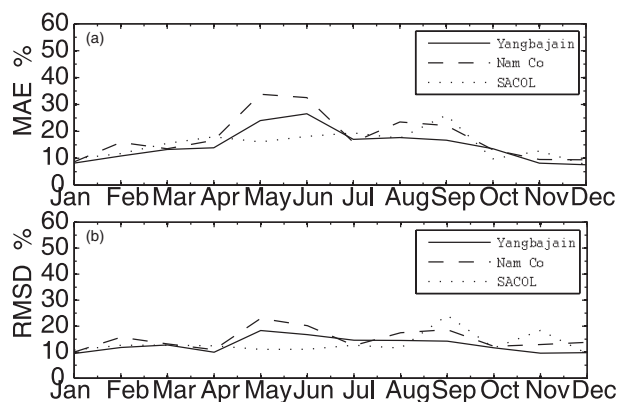


Fig. 4. The error of FLASHFlux/CERES DSSR for all all-sky days in every month: (a) mean absolute error; (b) root-mean-square deviation.

peak of the MAE (26.05%) in September. The RMSD remains at about 11%, with a highest value of 24.18% in September and second highest value of 18.39% in November.

The error varies at different sites with different surface properties. The error at SACOL is relatively stable over the whole year, which is probably related to the relatively stable cloud activity. At Yangbajain and Nam Co, the error in May and June is larger than that of other months. The peak error in May and June is associated with the large cloud amount during that time (Huo and LÜ, 2012). The large RMSD indicates that the spatial and temporal variability of clouds contributes to considerable uncertainty in May and June. The differences between the FLASHFlux and surface measurements are different among different sites. These differences are unstable and large over rugged terrain compared with relatively flat terrain, especially when cloud activity is highly frequent. The above results indicate large uncertainty in the coupling between 3D heterogeneous clouds and complex surface properties on radiative transfer processes. The complex surface properties can induce complex weather types and sky conditions, which eventually forms a complex physical role to affect the radiation transfer process.

3.2. The spatial variation of satellite-derived instantaneous DSSR

This subsection described the work using the SSF/CERES instantaneous orbit products. The coefficient of variability (CV), which is mainly used to compare the dispersion of the different groups, is the ratio of the standard deviation to the corresponding average of a set of data. In order to evaluate the effect of surface properties on the distribution of DSSR, three regions were chosen to obtain domain averages. These three regions were located at the same latitudes (26° – 40° N) but at different longitudes: eastern China–western Pacific (ECWP, 105° – 135° E), subtropical North Pacific (NP, 150° – 180° E), and the Tibetan Plateau (TP, 75° – 105° E). Based on digital elevation data at the resolution of 500 m from SRTM (Shuttle Radar Topography Mission),

NASA, Fig. 5 shows the elevation of the TP and ECWP region. The white region on the right represents the ocean. The NP region is characterized by sea surface and is not shown in Fig. 5. Clear-sky conditions were defined as occurring when the clear area percentage coverage at the subpixel resolution was greater than 99.9%. During the period 1 April 2009 to 31 March 2010, the monorail tracks within an hour that contained clear-sky sampling points (M) of more than 500 were chosen as our experimental database; the number of such tracks was 145 in the TP region, 190 in the ECWP region, and 54 in the NP region.

Figure 6 shows the variation of the spatial CV of DSSR in the 1 h track, plotted by the ordinal number of eligible tracks (N) from January to December on the horizontal axis and the CV on the vertical axis. The number above the horizontal axis represents the month corresponding to N , and some months are not marked in the figure because of the inexistence of eligible orbits or too few eligible tracks. These unmarked months include June, July and August for the TP region (Fig. 6a), and January for the NP region (Fig. 6c). The months between April and September are referred to as the summer half year, and others are referred to as the winter half year. If the monorail tracks within an hour that contained clear-sky sampling points of more than 800 were chosen, the number of such tracks was 56 in the TP region, 128 in the ECWP region, and 15 in the NP region. The distributions of the spatial CV for the sampling points of more than 800 were the same as those for the sampling points of more than 500, so the figures for the sampling points of more than 800 are not shown.

The CERES products do not fully account for the impact of the varied surface properties, especially the impact of complex topography. The errors in computing the radiative transfer can influence the DSSR results. There are two ways in which the surface influences the CV: one is the nature of the radiative transfer related to the surface, and the other is the limitation of the satellite inversion algorithm in resolving the sophisticated surface properties. It is hard to completely separate these two effects under current conditions. However, there are only slight differences between the “A” model products and the “B” model products in their spatial CVs of DSSR under clear-sky conditions (Fig. 6), which suggests that the DSSR error induced by the limitations of the satellite inversion algorithm has little impact on the CV. Therefore, the nature of the radiative transfer is the dominant factor in the occurrence of the different CV in the different regions. The influence of surface characteristics on the DSSR displays annual variation, and this annual variation presents the same pattern as the shape of the opening up of the parabolic in the three different areas. The annual variabilities of the CV in the TP and ECWP regions may be mainly attributable to the shading effect. The shading effect is relatively small when the solar altitude angle is high, which would lead to the lower CV in the summer half year. In the NP region, the wave changes may lead to the annual variability of the CV. The waves are closely related to the wind speeds. In winter, the NP region takes the brunt of the prevailing westerlies, which results in

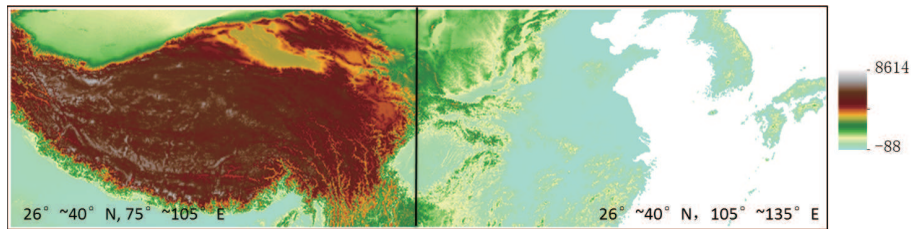


Fig. 5. Elevation (at the resolution of 500 m from SRTM, NASA) of the TP and ECWP regions (units: m). The white region on the right represents the ocean.

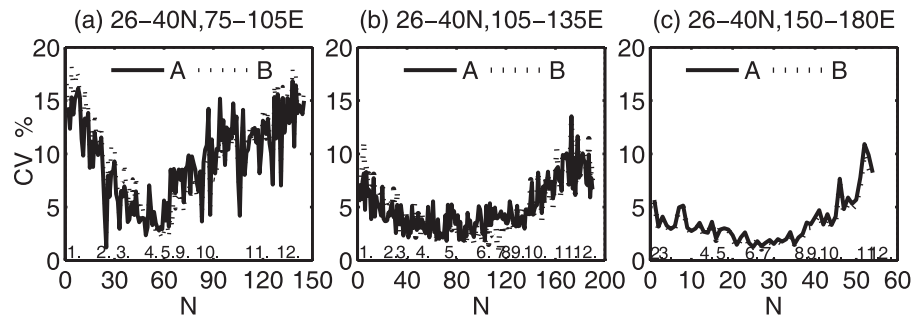


Fig. 6. Coefficient of spatial variation for SSF/CERES DSSR: (a) Tibetan Plateau (TP); (b) eastern China–western Pacific (ECWP); (c) subtropical North Pacific Ocean (NP). The number of clear pixels is larger than 500 in one hour on the satellite scanning track; “A” and “B” respectively represent the satellite data from the “A” model and “B” model. The horizontal axis shows the ordinal number of eligible tracks N from January to December. The number above the horizontal axis represents the month corresponding to N .

the high wind speeds. In summer, the wind speeds are relatively small in the NP region because of the influence of the subtropical high pressure. The CV ranges from about 1% to 17% in the TP. The overall ranges of CV in the ECWP and NP regions are very similar, and the CV varies from 1% up to 13%. The ranges of CV are similar in the NP and ECWP regions probably because the entire NP region and about half of the ECWP region are covered by ocean. The land surface of the ECWP region is much less variable than that of the TP region, while the underlying surface of the NP region is mainly affected by waves. The similar ranges of the CV in the ECWP and NP regions may indicate that the influence of huge waves on the CV can be as large as that of the land surface.

In the three regions within the same latitudes, solar radiation in the TP is the most strongly affected by the underlying surface conditions. Table 1 illustrates the spatial CV of DSSR in the three areas. In the situation of M being greater than 500, the average CV is 9.44% for the TP region, 4.95% for the ECWP region, and 3.49% for the NP region. In the situation of M being greater than 800, the average CV is 10.5% for the TP region, 5.11% for the ECWP region, and 3.55% for the NP region, respectively. The sunlight or solar fluxes that reach the surface can be physically grouped into the following five components: direct flux, diffuse flux, direct-reflected flux, diffuse-reflected flux, and coupled flux. The direct-reflected flux, which consists of photons directly from the sun without encountering scattering, and are

Table 1. Statistics for the DSSR under clear-sky conditions.

		Mean ($W m^{-2}$)	Standard deviation ($W m^{-2}$)	CV
$M \geq 500$	TP	686	60.4	9.44%
	ECWP	733	33.0	4.95%
	NP	848	27.6	3.49%
$M \geq 800$	TP	670	66.5	10.5%
	ECWP	724	33.8	5.11%
	NP	842	28.0	3.55%

Note: The mean CV of each region is the averaged CV of all eligible tracks. The mean DSSR and standard deviation of each region are obtained in the same way as the mean CV.

subsequently reflected by surrounding terrain, is the dominant component contributing to the different DSSR between the flat surface and the surface with complex topography (Lee et al., 2013). As can be seen from the above, the impact of underlying surface conditions is the lowest in the NP region and the greatest in the TP region, which is about twice as large as that in the other two regions.

Figure 7 demonstrates the variation of DSSR in one hour for several satellite scanning tracks when M is greater than 800. The days chosen in Figs. 6a–f are very close, and the DSSR for a large region as a whole has no obvious change in one or two days, so the variations are comparable. Figures 7a and e show the variation in the TP and NP regions on the

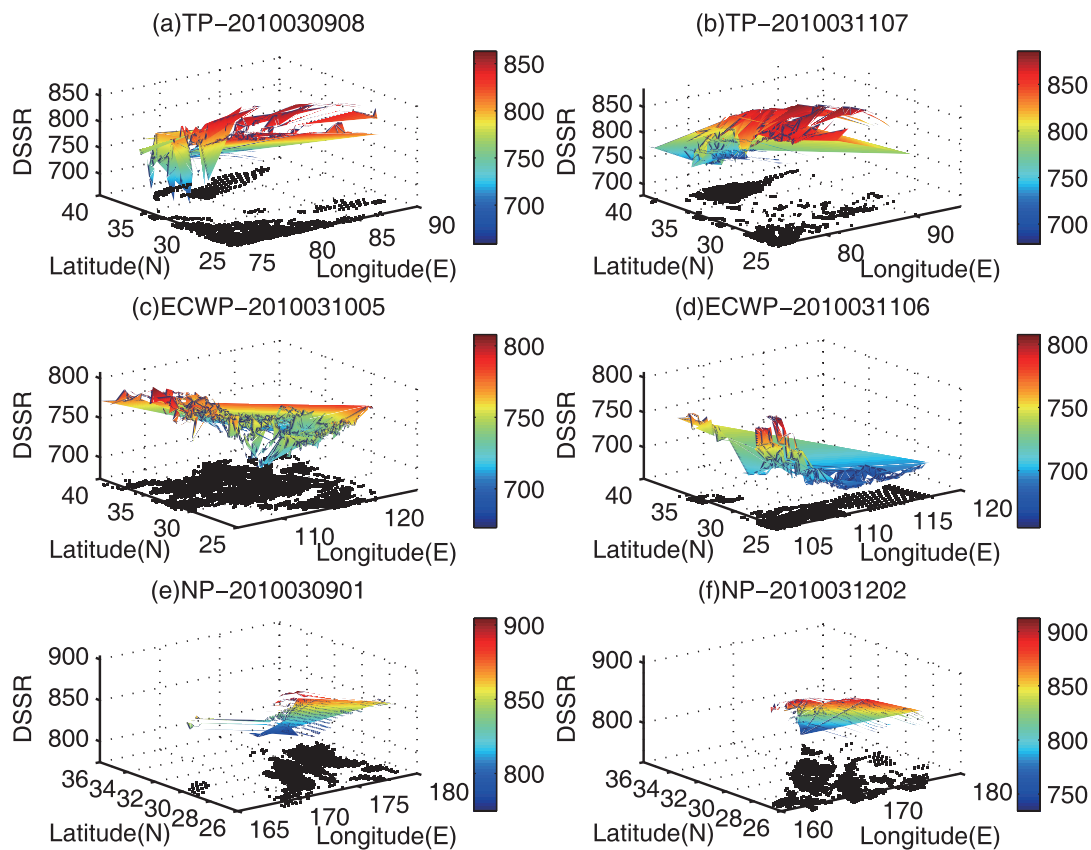


Fig. 7. The variation of SSF/CERES DSSR in one hour on the satellite scanning track (units: W m^{-2}): (a, b) Tibetan Plateau (TP); (c, d) Eastern China–western Pacific (ECWP); (e, f) subtropical North Pacific Ocean (NP). Both the height in the vertical direction and the coloring stands for the value of DSSR. The dark spots at the bottom of each panel represent the locations under clear skies. Taking (a) as an example, the label “2010030908” means between 0800 and 0859 on 9 March 2010 UTC.

same day (9 March 2010 UTC), respectively. The clear-sky sampling points in the monorail track within an hour are 1256 for Fig. 7a, and 814 for Fig. 7e. The CV of DSSR is 5.98% for the TP region and 3.17% for the NP region. Although the distribution of clear-sky sampling points can affect the CV, the surface properties still contribute the most to the DSSR and its CV. Figures 7b and f are for two tracks with similar clear-sky sampling points (1036 and 1091, respectively) on nearby days. The spatial CV of DSSR is 6.95% in the TP region and 4.10% in the NP region. Figures 7c and d show the spatial variation of DSSR within one hour for two tracks in the ECWP region. M is 2722 for Fig. 7c and 851 for Fig. 7d. The CV is 2.55% and 4.95%, respectively. The above case analyses show that the underlying surface properties affect the distribution of DSSR the most in the TP region.

3.3. Simulation by the I3RC model

Shortwave flux transmittance (T) is the ratio of the surface horizontal solar radiation to extraterrestrial radiation (Liou, 2002). Under the concurrence of variable surface albedo and 3D clouds, what is the effect of surface albedo on the shortwave flux transmittance? As an example, Fig. 8 shows the distributions of the shortwave flux transmittance

of stratocumulus clouds. Figures 8a–d are for the wavelength of $0.675 \mu\text{m}$, and Figs. 8e–h are for the wavelength of $2.13 \mu\text{m}$. For each simulation at a certain wavelength, the surface albedo was 0.0 for Figs. 8a and e, 0.2 for Figs. 8b and f, 0.4 for Figs. 8c and g, and 0.6 for Figs. 8d and h. For the regions with white color, the transmittance is greater than 1.0, which means that the enhancement of the radiation caused by cloud cover is more evident than the reducing effect. We know that such a phenomenon is mainly induced by scattered radiation resulting from the underlying surface and inhomogeneous structure of clouds in principle. From the figures, we conclude that the distributions of shortwave radiation transmittance in the three domains are similar, which is mainly caused by the structure of clouds. The average T at $0.675 \mu\text{m}$ is 0.686, 0.745, 0.815 and 0.900 for a surface albedo of 0.0, 0.2, 0.4 and 0.6, and at $2.13 \mu\text{m}$ it is 0.512, 0.548, 0.589 and 0.638, respectively. It is clear that the shortwave flux transmittance increases as the surface albedo increases.

Another example is for the impact of cumulus cloud on the distribution of the shortwave flux transmittance (Fig. 9). Figures 9a–d are at $0.675 \mu\text{m}$, and Figs. 9e–h are at $2.13 \mu\text{m}$. The average T at $0.675 \mu\text{m}$ is 0.900, 0.929, 0.959, and 0.992 for a surface albedo of 0.0, 0.2, 0.4 and 0.6, respec-

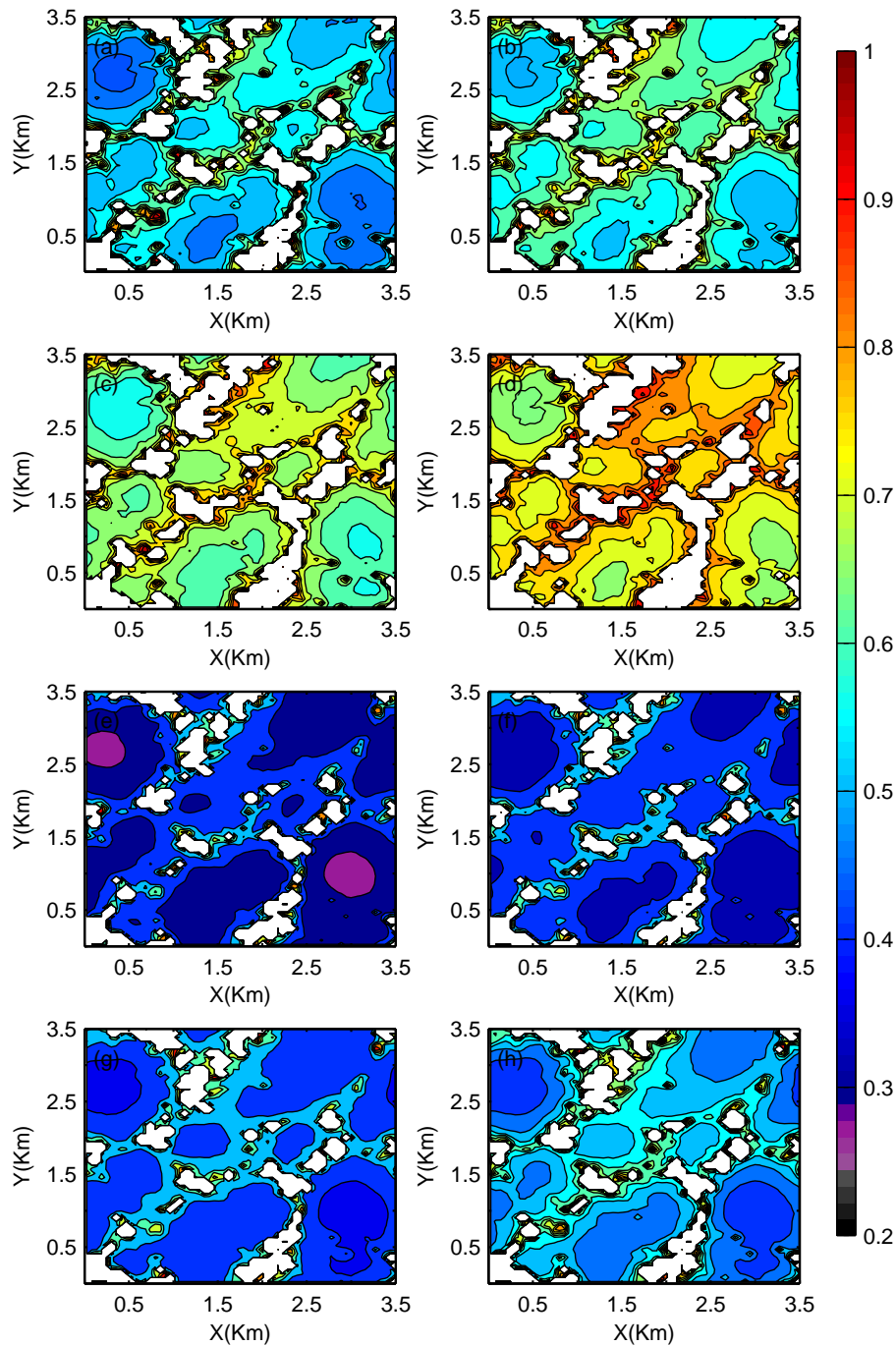


Fig. 8. Simulated shortwave flux transmittance of stratocumulus cloud at wavelengths (a–d) 0.675 μm and (e–h) 2.13 μm . The surface albedos are 0.0 in (a, e), 0.2 in (b, f), 0.4 in (c, g) and 0.6 in (d, h).

tively, and at 2.13 μm it is 0.860, 0.880, 0.901 and 0.923, respectively. For cumulus cloud, the effects of surface albedo on downward shortwave radiation flux are weaker than for stratocumulus cloud. This is because the stratocumulus cloud field has a much more complex structure than that of cumulus cloud. Surface properties have a stronger effect on solar radiation under the sky of more complex 3D clouds. The largest effect occurs in regions with cloud gaps. This is mainly attributed to the increase of the diffuse radiation, while the di-

rect solar radiation component is almost unaffected. If the spatial changes of cloud properties (e.g. cloud optical thickness, liquid water content, effective particle radius, cloud coverage and geometry) are more complex, the role of surface albedo on DSSR is stronger. At the same time, we can see that DSSR will increase as surface albedo increases. As the surface albedo increases, more photons will be reflected to the sky instead of reaching the ground, and participate in the processes of multiple scattering. A proportion of those re-

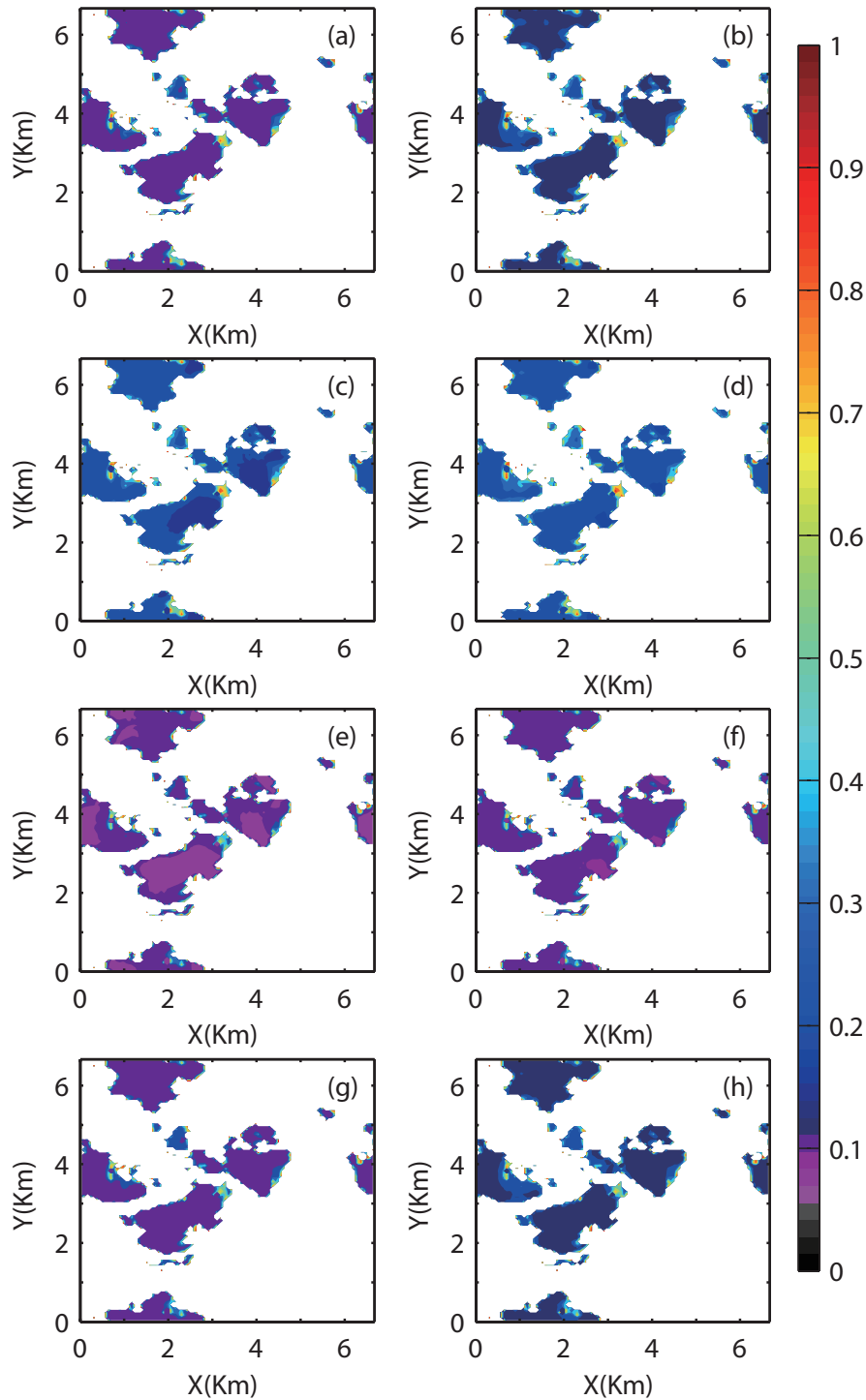


Fig. 9. Simulated shortwave flux transmittance of cumulus cloud at wavelengths (a–d) 0.675 μm and (e–h) 2.13 μm . The surface albedos are 0.0 in (a, e), 0.2 in (b, f), 0.4 in (c, g) and 0.6 in (d, h).

flected photons will transfer to the ground through a complex physical process.

Previous studies on surface albedo have paid much more attention to its effect on the upward surface shortwave radiation than its effect on the DSSR (e.g., Li et al., 1993; Gupta et al., 2001; Ma and Pinker, 2012; Qin et al., 2012). Our study

shows that surface albedo has an important role in the value of DSSR itself. Given the importance of the upward surface shortwave radiation based on surface albedo and DSSR, it is necessary to consider the effect of surface albedo on the surface radiation budget. Surface albedo is a dynamic parameter. It can change not only with the variation of surface

conditions, such as the physical and chemical properties of soil, but also with the sun's angle. Surface albedo itself is complex and uncertain. At present, the problem of the error due to surface albedo in the satellite inversion and radiative transfer algorithm is a challenge in the field of atmospheric science. Further study is still needed.

4. Conclusion and discussion

4.1. Conclusion

As a basic problem in the earth–atmosphere system, detailed studies of the radiative transfer process contribute to further research on climate change and the physics of remote sensing. In the TP region, its protruding nature with high elevation and complex surface properties results in equally complex weather and cloud systems. As a result, present radiative transfer models and satellite inversion algorithms cannot meet the necessary requirements. Satellite remote sensing has become more and more widely used in the geosciences. However, satellite data should be evaluated against *in situ* observations before being used. The TP is characterized by high elevation and complex surface properties, and thus acts as a useful benchmark for evaluating satellite data. *In situ* observations at Yangbajain, Nam Co, and SACOL were adopted in this study to evaluate FLASHFlux satellite data. The effects of surface properties on the DSSR were analyzed by comparing the TP, ECWP and NP regions. The I3RC model was used to study the effects of surface albedo on the DSSR. The main results can be summarized as follows:

(1) Under clear-sky conditions, the satellite products and *in situ* data are consistent with a correlation of 0.992 at Yangbajain, 0.991 at Nam Co site, and 0.998 at SACOL. The mean absolute error of satellite-estimated products is about 6.7% at Yangbajain, 6.3% at Nam Co, and 3.4% at SACOL. Under all-sky conditions, the error increases significantly because the present algorithms ignore 3D cloud properties. The quality of the satellite inversion products is spatially dependent, and it tends to be better for smoother terrain. The error increases and becomes more variable with the increasing complexity of surface properties.

(2) The CV was used to evaluate the effect of surface properties on the distribution of DSSR. The work was performed by choosing three regions located at the same latitudes (26°–40°N), including the TP region (75°–105°E), the ECWP region (105°–135°E), and the NP region (150°–180°E). The CV has an annual cycle, which is higher in the winter half year and lower in the summer half year. The maximum CV reaches about 17% in the TP region, and about 13% in the other two regions. When the clear-sky sampling points of the monorail track within an hour are greater than 500, the average CV is 9.44% for the TP region, 4.95% for the ECWP region, and 3.49% for the NP region. When the clear-sky sampling points are greater than 800, the averaged CV is 10.5%, 5.11% and 3.55%, respectively. The impact of underlying surface features in the TP region is about twice as large as in the ECWP or NP regions.

(3) The I3RC numerical simulations showed that surface albedo affects DSSR dramatically. DSSR increases as surface albedo increases, and the impact of surface albedo on DSSR is larger if the spatial distribution of clouds is more non-uniform. Surface albedo is just one of the parameters of surface properties. It is necessary to consider the effect of surface albedo on the surface radiation budget.

4.2. Discussion

Current satellite products face great challenges over the TP because of the complex surface and sky conditions. Surface properties dramatically affect the distribution of DSSR over the TP, which in turn will modulate the energy cycle and further lead to a series of climatic and meteorological consequences. The present study qualitatively and quantitatively indicated that the effect of surface features is an absolute restriction for the precision of current radiative transfer models and satellite inversion algorithms. In areas with a complex surface, the variability of that underlying surface and its radiative properties combine to generate complicated spatial and temporal patterns of surface radiation budgets. Under clear-sky conditions, shortwave surface effects can lead to surface temperature differences of up to 2.5 K, and longwave effects to differences of up to 1 K (Manners et al., 2012). The TP has very different characteristics of DSSR compared to other regions. More attention should be paid to the effect of the underlying surface on the surface radiation balance.

In terms of the effect of surface properties, most previous studies have simply performed their work under clear-sky conditions (e.g. Liou et al., 2007; Manners et al., 2012; Lee et al., 2013). However, the Earth's average cloud fraction is about two thirds (Maddux et al., 2010), and the complexity of surface properties can induce equally complex weather types and sky conditions. Complex surfaces and 3D clouds coexist most of the time. In our simulation, only the surface albedo effect was investigated under the sky with 3D clouds because of the limitation of the current I3RC Monte Carlo code. Our simulation showed that the impact of surface albedo on DSSR is larger if the spatial distribution of clouds is more non-uniform. The problem will be more complex if the topographic effect is added into the radiative transfer model. In the future, we intend to perform studies of the topographic effect by improving the I3RC Monte Carlo model, or by using other effective models. The present work can be used as a foundation upon which we can build and think about how to extract the surface shortwave radiation values by using more accurate methods and satellite data. It is imperative to establish inhomogeneous surface–atmosphere coupling into radiative transfer models.

Acknowledgements. This research was supported by the National Natural Science Foundation of China (Grant No. 41127901) and the Strategic Priority Research Program–Climate Change: Carbon Budget and Relevant Issues (Grant No. XDA05040300). The authors would like to thank Profs. HUANG Jian-Ping, ZHANG Wu, MA Yao-Ming, XUAN Yue-Jian, and CHEN Hong-Bin for their provision of *in situ* data. The authors would also like to thank Prof.

Tamas VARNAI and Prof. Robert PINCUS for their many suggestions and discussions on the Monte Carlo model.

REFERENCES

- Cahalan, R. F., and Coauthors, 2005: The I3RC: Bringing together the most advanced radiative transfer tools for cloudy atmospheres. *Bull. Amer. Meteor. Soc.*, **86**(9), 1275–1293.
- Cong, Z. Y., S. C. Kang, A. Smirnov, and B. Holben, 2009: Aerosol optical properties at Nam Co, a remote site in central Tibetan Plateau. *Atmos. Res.*, **92**(1), 42–48.
- Dubayah, R. C., and S. Loechel, 1997: Modeling topographic solar radiation using GOES data. *J. Appl. Meteor.*, **36**(2), 141–154.
- Dubayah, R. C., and P. M. Rich, 1995: Topographic solar radiation models for GIS. *Int. J. Geographical Inform. Syst.*, **9**(4), 405–419.
- Evans, K. F., and A. Marshak, 2005: Numerical methods. *3D Radiative Transfer in Cloudy Atmospheres*. A. Marshak and A. B. Davis, Eds., Springer, Berlin, 261–274.
- Geiger, M., L. Diabate, L. Menard, and L. Wald, 2002: A web service for controlling the quality of measurements of global solar irradiation. *Solar Energy*, **73**(6), 475–480.
- Gui, S., S. L. Liang, and L. Li, 2009: Validation of surface radiation data provided by the CERES over the Tibetan Plateau. *2009 17th International Conference on Geoinformatics*, Fairfax, VA, 1–6.
- Gui, S., S. L. Liang, K. C. Wang, and L. Li, 2010: Assessment of three satellite-estimated land surface downwelling shortwave irradiance data Sets. *IEEE Geosci. Remote Sens. Lett.*, **7**(4), 776–780.
- Gupta, S. K., D. P. Kratz, Jr. P. W. Stackhouse, and A. C. Wilber, 2001: The Langley parameterized shortwave algorithm (LPSA) for surface radiation budget studies (version1.0). NASA/TP-2001-211272.
- Hayasaka, T., K. Kawamoto, G. Shi, and A. Ohmura, 2006: Importance of aerosols in satellite-derived estimates of surface shortwave irradiance over China. *Geophys. Res. Lett.*, **33**, L06802, doi:10.1029/2005GL025093.
- Helbig, N., H. Löwe, and M. Lehning, 2009: Radiosity approach for the surface radiation balance in complex terrain. *J. Atmos. Sci.*, **66**, 2900–2912.
- Houborg, R., H. Soegaard, W. Emmerich, and S. Moran, 2007: Inferences of all-sky solar irradiance using Terra and Aqua MODIS satellite data. *Int. J. Remote Sens.*, **28**(20), 4509–4535.
- Huang, J. Y., 2004: *Meteorological Statistical Analysis and Forecast Method*. China Meteorological Press, Beijing, 298 pp. (in Chinese)
- Huo, J., and D. R. Lü, 2012: Cloud amount analysis at Yangbajing of Tibet in 2009–2010 using all-sky images. *Climatic and Environmental Research*, **17**(4), 393–399. (in Chinese)
- Kang, S., S. Kim, and D. Lee, 2002: Spatial and temporal patterns of solar radiation based on topography and air temperature. *Canadian Journal of Forest Research*, **32**(3), 487–497.
- Kim, H. Y., and S. L. Liang, 2010: Development of a hybrid method for estimating land surface shortwave net radiation from MODIS data. *Remote Sens. Environ.*, **114**, 2393–2402.
- Kurosaki, Y., and F. Kimura, 2002: Relationship between topography and daytime cloud activity around Tibetan Plateau. *J. Meteor. Soc. Japan*, **80**(6), 1139–1355.
- Kuwagata, T., A. Numaguti, and N. Endo, 2001: Diurnal variation of water vapor over the central Tibetan Plateau during summer. *J. Meteor. Soc. Japan*, **79**, 401–418.
- Lee, W. L., K. N. Liou, and C. C. Wang, 2013: Impact of 3-D topography on surface radiation budget over the Tibetan Plateau. *Theor. Appl. Climatol.*, **113**, 95–103.
- Li, Z., H. G. Leighton, K. Masuda, and T. Takashima, 1993: Estimation of SW flux absorbed at the surface from TOA reflected flux. *J. Climate*, **6**(2), 317–330.
- Liou, K. N., 2002: *An Introduction to Atmospheric Radiation*. 2nd ed., Academic Press, Boston, 583 pp.
- Liou, K. N., W. Lee, and A. Hall, 2007: Radiative transfer in mountains: Application to the Tibetan Plateau. *Geophys. Res. Lett.*, **34**, L23809, doi: 10.1029/2007GL031762.
- Loeb, N. G., N. M. Smith, S. Kato, W. F. Miller, S. K. Gupta, P. Minnis, and B. A. Wielicki, 2003: Angular distribution models for top-of-atmosphere radiative flux estimation from the clouds and the Earth's radiant energy system instrument on the Tropical Rainfall Measuring Mission satellite. Part I: Methodology. *J. Appl. Meteor.*, **42**, 240–265.
- Ma, Y., and R. T. Pinker, 2012: Modeling shortwave radiative fluxes from satellites. *J. Geophys. Res.*, **117**, D23202, doi: 10.1029/2012JD018332.
- Ma, Y., and Coauthors, 2005: Diurnal and inter-monthly variation of land surface heat fluxes over the central Tibetan Plateau area. *Theor. Appl. Climatol.*, **80**, 259–273.
- Maddux, B., S. A. Ackeman, and S. Platnick, 2010: Viewing geometry dependencies in MODIS cloud products. *J. Atmos. Oceanic Technol.*, **27**(9), 1519–1528.
- Manners, J., S. B. Vosper, N. Roberts, 2012: Radiative transfer over resolved topographic features for high-resolution weather prediction. *Quart. J. Roy. Meteor. Soc.*, **138**, 720–733.
- Moeng, C. H., and Coauthors, 1996: Simulation of a stratocumulus-topped planetary boundary layer: Intercomparison among different numerical codes. *Bull. Amer. Meteor. Soc.*, **77**(2), 261–278.
- Ohring, G., B. Wielicki, R. Spencer, B. Emery, and R. Datla, 2005: Satellite instrument calibration for measuring global climate change. *Bull. Amer. Meteor. Soc.*, **86**, 1303–1314.
- Pincus, R., and K. F. Evans, 2009: Computational cost and accuracy in calculating three-dimensional radiative transfer: Results for new implementations of Monte Carlo and SHDOM. *J. Atmos. Sci.*, **66**, 3131–3146.
- Qin, J., K. Yang, S. Liang, and W. Tang, 2012: Estimation of daily mean photosynthetically active radiation under All-Sky conditions based on relative sunshine data. *J. Appl. Meteor. Climatol.*, **51**, 150–160.
- Ryu, Y., S. Kang, S. K. Moon, and J. Kim, 2008: Evaluation of land surface radiation balance derived from moderate resolution imaging spectroradiometer (MODIS) over complex terrain and heterogeneous landscape on clear sky days. *Agric. Forest. Meteorol.*, **148**(10), 1538–1552.
- Spencer, J. W., 1971: Fourier series representation of the position of the sun. *Search*, **2**, 172.
- Stevens, B., and D. H. Lenschow, 2001: Observations, experiments, and large eddy simulation. *Bull. Amer. Meteor. Soc.*, **82**(2), 283–294.
- Stöckli, R., 2013: The HelioMont Surface Solar Radiation Processing. Scientific Report MeteoSwiss, No. 93, 122 pp.
- Stroeve, J., J. E. Box, F. Gao, S. Liang, A. Nolin, and C. Schaaf, 2005: Accuracy assessment of the MODIS 16-day albedo product for snow: Comparisons with Greenland in situ mea-

- surements. *Remote Sens. Environ.*, **94**(1), 46–60.
- Wang, K. C., X. J. Zhou, J. M. Liu, and M. Sparrow, 2005: Estimating surface solar radiation over complex terrain using moderate-resolution satellite sensor data. *Int. J. Remote Sens.*, **26**(1), 47–58.
- Wang, L. D., D. R. Lü, and W. X. Zhang, 2013: Study on characteristic of solar radiation at Nam Co and Yangbajain in Qinghai-Xizang Plateau. *Plateau Meteorology*, **32**(2), 315–326. (in Chinese)
- Wang, L. D., D. R. Lü, and J. Huo, 2014: Observation and simulation of abnormal transmittance over Yangbajing, Tibet. *Atmospheric and Oceanic Sciences Letters*, **7**, 190–197, doi: 10.3878/j.issn.1674-2834.13.0086.
- Wang, S., R. F. Grant, D. L. Verseghy, and T. A. Blac, 2002: Modelling carbon dynamics of boreal forest ecosystems using the Canadian land surface scheme. *Climatic Change*, **55**(4), 451–477.
- Yang, K., T. Koike, P. Stackhouse, C. Mikovitz, and S. J. Cox, 2006: An assessment of satellite Surface radiation Products for highlands with Tibet instrumental data. *Geophys. Res. Lett.*, **33**, L22403, doi: 10.1029/2006GL027640.
- Yang, K., R. T. Pinker, Y. M. Ma, T. Koike, M. M. Wonsick, S. J. Cox, Y. C. Zhang, and P. Stackhouse, 2008: Evaluation of satellite estimates of downward shortwave radiation over the Tibetan Plateau. *J. Geophys. Res.*, **113**, D17204, doi: 10.1029/2007JD009736.
- Yang, K., J. He, W. J. Tang, J. Qin, and C. C. K. Cheng, 2010: On downward shortwave and longwave radiations over high altitude regions: Observation and modeling in the Tibetan Plateau. *Agric. Forest. Meteor.*, **150**(1), 38–46.
- Zhang, Y. C., W. B. Rossow, and Jr. P. W. Stackhouse, 2006: Comparison of different global information sources used in surface radiative flux calculation: Radiative properties of the near-surface atmosphere. *J. Geophys. Res.*, **111**, D13106, doi: 10.1029/2005JD006873.
- Zhang, Y. C., W. B. Rossow, and Jr. P. W. Stackhouse, 2007: Comparison of different global information sources used in surface radiative flux calculation: Radiative properties of the surface. *J. Geophys. Res.*, **112**, D01102, doi: 10.1029/2005JD007008.